J. Plasma Phys. (2021), *vol*. 87, 905870313
Published by Cambridge University Press
doi:10.1017/S0022377821000660

Compton-driven beam formation and magnetization via plasma microinstabilities

Bertrand Martinez [1],†, **Thomas Grismayer**[1] **and Luís O. Silva**[1]

[1]GoLP/Instituto de Plasmas e Fusão Nuclear, Instituto Superior Técnico, Universidade de Lisboa, 1049-001 Lisbon, Portugal

(Received 23 February 2021; revised 2 June 2021; accepted 9 June 2021)

Compton scattering of gamma rays propagating in a pair plasma can drive the formation of a relativistic electron positron beam. This process is scrutinized theoretically and numerically via particle-in-cell simulations. In addition, we determine in which conditions the beam can prompt a beam-plasma instability and convert its kinetic energy into magnetic energy. We argue that such conditions can be met at the photosphere radius of bright gamma-ray bursts.

Key words: plasma instabilities

1. Introduction

The interaction of gamma rays with a pair plasma is a fundamental problem in astrophysics. For instance, it is present in the context of gamma-ray bursts (GRBs). The latter involve the explosion of a stellar mass object, where energy is expelled in the form of a relativistic ejecta. As this ejecta propagates, its interaction with the ambient medium generates a strong emission which is detected by satellites as well as ground-based observatories. Recent efforts demonstrated emission over a large range of frequencies including the radio, optical, X-ray and gamma-ray bands, up to TeV energies (Acciari *et al.* 2019).

For most GRBs, the temporal evolution of the observations shows that their spectra consist of two parts, a prompt emission followed by an afterglow. The prompt emission of a GRB is defined as an initial emission phase in the keV–MeV band, which lasts for a few milliseconds to several minutes. The afterglow is a counterpart of the prompt emission extending in the optical and radio ranges and its duration can span from a few hours to several days. While it is acknowledged that a large part of the afterglow can be attributed to a forward external shock driven by the ejecta propagating in the ambient medium (Meszaros & Rees 1997), the origin of the prompt emission is not fully understood yet. The main reason is that there remains unanswered questions related to the composition of the ejecta, how its energy is dissipated and how particles are accelerated.

All models agree that there is an ejecta formed by a compact object of radius $\sim 10^7$ cm. This ejecta is a relativistic plasma in expansion. Most of its energy comes from photons, but it also contains pairs, an unknown fraction of baryons that may even be magnetized. At this early stage of expansion the relativistic plasma is so dense that photons cannot

† Email address for correspondence: bertrand.martinez@tecnico.ulisboa.pt

escape. At the photospheric radius $\sim 10^{12}$ cm, its density has decreased enough to enable a fraction of the gamma rays to propagate in the ambient medium (Cavallo & Rees 1978). One of the pending questions related to GRBs is how does the ejecta dissipate its energy above such a large distance of $\sim 10^{12}$ cm? This question has been addressed in two ways, as detailed in a recent review on GRBs (Kumar & Zhang 2015).

First, researchers proposed models that describe the overall evolution of the ejecta. The most used is the hot fireball model which assumes that the energy of the ejecta is dissipated at the photosphere radius and in internal/external shocks (Narayan, Paczynski & Piran 1992; Rees & Meszaros 1994; Piran 2005). However, it should be mentioned that some GRB spectra are better explained with a model assuming a magnetized ejecta, where the energy is dissipated via current-driven instabilities (Lyutikov 2006; Zhang & Yan 2010). The gamma-ray emission processes are manifold and are widely discussed in these models. The processes are usually synchrotron (Meszaros & Rees 1993; Rees & Meszaros 1994), inverse Compton (Gruzinov & Mészáros 2000) or inverse Compton up-scattering of synchrotron photons by high-energy electrons (synchrotron–self-Compton). In the Klein–Nishina regime, the Compton process is also held responsible for a bulk plasma acceleration called Compton drag or radiative acceleration (Madau & Thompson 2000; Thompson & Madau 2000). Our work here goes beyond these, by assuming that collective plasma processes can be triggered as the energetic photons propagate through the plasma. On another hand, some hadronic processes (Bethe–Heitler and photopion) are discussed as possible sources of high-energy positrons, which then radiate gamma rays via synchrotron. Pair production processes are also proven to play a significant role in the development of key features of GRBs such as their high radiative efficiency (Stern 2003) or their flat spectrum from the infrared to the ultraviolet (Beloborodov 2005).

Second, researchers also performed numerical simulations of basic plasma processes in the extreme conditions of GRBs using particle-in-cell (PIC) simulations. Employing this framework enables one to account for collective plasma dynamics, radiative processes and, more importantly, for any dynamical feedback between the two. The first example relevant in the context of GRBs (Medvedev & Loeb 1999) is the simulation of relativistic collisionless shock formation by the Weibel instability (Silva *et al.* 2003) and the subsequent Fermi-type particle acceleration (Spitkovsky 2008; Martins *et al.* 2009). The second example is particle acceleration in magnetic reconnection regions (Mehlhaff *et al.* 2020),which is known to be of interest for GRBs (Uzdensky 2011). The third example is electron acceleration in Compton-driven plasma wakefields during the GRB interaction with its circumburst medium (CBM) (Frederiksen 2008; Del Gaudio *et al.* 2020*a*).

In his study, Frederiksen considers the interaction of a Planckian photon distribution with a tenuous plasma (Frederiksen 2008). The photon energy lies between 30 keV and 3 MeV and he observes electron acceleration in a plasma wakefield. According to the author, this wakefield is excited by an electrostatic force acting to restore the charge separation induced by Compton deflections. In contrast to this work, our investigation focuses on a regime where the Compton cross-section is beamed above 10 MeV. In addition, we consider a range where Compton scattering prevails over the Bethe–Heitler pair production ($\gamma e \rightarrow e^+e^-e$) for energies below 100 MeV. Formulae for all these processes can be found in the paper by Lightman (1982). For this gamma-ray range of 10–100 MeV, one expects Compton scattering to deflect electrons mainly forward such that they form a relativistic beam (Del Gaudio *et al.* 2020*a*).

In light of these previous results, we investigate the interaction of gamma rays (10–100 MeV) with a background pair plasma. In § 2, with the support of a one-dimensional (1-D) theoretical model and PIC simulations, we clarify how a gamma-ray beam (10–100 MeV)

https://doi.org/10.1017/S0022377821000660 Published online by Cambridge University Press

propagating in a pair plasma can drive the formation of a relativistic and dense electron positron beam via Compton scattering. In § 3, we specify under which conditions the pair beam can trigger a beam-plasma instability, thus generating a small-scale magnetic field whose extent is discussed. Section 4 confirms the robustness of this process for various photon sources. Finally, we argue in § 5 that these conditions can be met for radii r such that $r \geq r_{\rm ph}$, with $r_{\rm ph}$ the photospheric radius of a GRB.

2. Pair beam formation

We first discuss a simplified physical picture. Let us consider a semi-infinite gamma-ray beam of density $n_{\omega 0}$ with a monoenergetic distribution. We denote the photon energy normalized by the electron rest mass as $\epsilon = \hbar\omega/mc^2$. The photon beam propagates along the x direction in an infinite cold pair plasma at rest, with density n_{p0} associated with an angular frequency ω_p. In the frame of this work, we focus on the energy range $1 \ll \epsilon < 1/\alpha_f = 137$, where α_f denotes the fine structure constant. In this range, Compton scattering prevails over the two-photon Breit–Wheeler process and pair creation in the Coulomb field of an electron or positron (Lightman 1982).

The formation process of the pair beam relies on the beaming of the Compton cross-section for high-energy photons. Let us consider an electron at rest experiencing Compton deflection from a gamma ray of energy ϵ, with $\mathrm{d}\sigma_{\rm kn}/\mathrm{d}\Omega$ and $\sigma_{\rm kn}(\epsilon)$ the angular-differential and total Compton cross-sections (Klein & Nishina 1928), and θ the polar angle associated with Ω, the photon angle after one scattering. The Lorentz factor of the electron after the deflection γ can be deduced from the energy and momentum balance as $\gamma/\epsilon = 1 + 1/\epsilon - 1/[1 + \epsilon(1 - \cos\theta)]$. We introduce ϕ the angle between the deflected electron momentum and the incident photon direction and obtain $\mathrm{cotan}(\phi) = (1 + \epsilon)\tan(\theta/2)$. Averaging these quantities over the Compton angular cross-section, we obtain for $\epsilon \gg 1$, $\langle\gamma\rangle_\Omega \simeq \epsilon$ and $\langle\sin^2\phi\rangle_\Omega \simeq 4/\epsilon$ (Blumenthal & Gould 1970). This shows that there is a simultaneous beaming of photons, electrons and positrons centred on the direction of the incident gamma ray. We will discuss later the effects induced by a more realistic gamma-ray beam distribution.

We assume that the longitudinal momentum of the pair beam (p_x) can be approximated by its average over the Compton cross-section $p_x \simeq \sqrt{\langle p_x^2\rangle_\Omega}$, and we define the transverse momentum spread induced by Compton scattering as $\Delta p_\perp = \sqrt{\langle p_\perp^2\rangle_\Omega}$. For $\epsilon \gg 1$,

$$\frac{p_x}{mc} \simeq \epsilon \quad \text{and} \quad \frac{\Delta p_\perp}{mc} \simeq \sqrt{\frac{7\epsilon}{6\ln\epsilon}}. \tag{2.1a,b}$$

Equation (2.1*a*,*b*) shows that the deflected electron energy can be as high as the incoming photon energy and that the transverse momentum spread of the pair beam is typically a few percent of its longitudinal momentum $\Delta p_\perp/p_x \simeq 5$–$20\,\%$ for $1 \ll \epsilon < 1/\alpha_f$.

The density of the photons decreases as they are scattered at a frequency $\tau_\omega^{-1} = 2n_{p0}c\sigma_{\rm kn}$. It thus follows that $\mathrm{d}n_\omega/\mathrm{d}t = -n_\omega/\tau_\omega$. The solution reads $n_\omega/n_{\omega 0} = \exp(-t/\tau_\omega)$. In the high-energy limit $\epsilon \gg 1$, one has $\sigma_{\rm kn}(\epsilon) \simeq \pi r_e^2 \ln(\epsilon)/\epsilon$, where r_e is the classical electron radius. As a result, the photon density can be approximated as constant $n_\omega/n_{\omega 0} \simeq 1$, where in fact $\omega_p\tau_\omega \propto r_e^{-3/2} n_{p0}^{-1/2}\epsilon/\ln(\epsilon) \gtrsim 10^{11}$ for any plasma density $n_{p0} \leq 10^{18}\ \mathrm{cm}^{-3}$, a conservative upper bound for astrophysical systems.

We now consider a more detailed model for the pair beam formation. Let us denote $n_p(x, t)$ as the background plasma density. The electrons (and positrons) of the beam are those experiencing at least one Compton scattering. Their density is denoted as $n_b(x, t)$ and they have a velocity v_b. At the initial time $t = 0$, we assume that the photons are located in the $x < 0$ half-space and propagate toward the background plasma at rest in the other

https://doi.org/10.1017/S0022377821000660 Published online by Cambridge University Press

half-space $x > 0$. The evolution of the background plasma density (beam density) is given by the continuity equation with a source term accounting for a depletion (loading) at the Compton frequency $\nu = \sigma_{\rm kn} c n_\omega$

$$\left.\begin{aligned} \partial_t n_p + \boldsymbol{\nabla} \cdot (n_p \boldsymbol{v}_p) &= -\sigma_{\rm kn} c n_\omega n_p \\ \partial_t n_b + \boldsymbol{\nabla} \cdot (n_b \boldsymbol{v}_b) &= \sigma_{\rm kn} c n_\omega n_p \end{aligned}\right\}. \tag{2.2}$$

We introduce the Heaviside function H, along with the variables ξ, τ defined as $\xi = ct - x$ and $\tau = t$. The background plasma is assumed to be at rest during the interaction ($\boldsymbol{v}_p = 0$), and the beam to have a constant velocity $\boldsymbol{v}_b = v_x \boldsymbol{x} = c\beta_x \boldsymbol{x}$. The evolution of the background plasma and beam densities simplifies to

$$[c\partial_\xi + \partial_\tau] n_p(\xi, \tau) = -\nu n_p(\xi, \tau)[H(\xi) - H(\xi - ct)], \tag{2.3}$$

$$[(c - v_x)\partial_\xi + \partial_\tau] n_b(\xi, \tau) = \nu n_p(\xi, \tau)[H(\xi) - H(\xi - ct)]. \tag{2.4}$$

We first solved (2.3) by assuming the solution is of the form $f(\xi)g(\tau)$. As far as (2.4) is concerned, its solution was derived using the method of Laplace transform. The solutions are obtained for all $\xi \leq c\tau$ as

$$n_p(\xi, \tau) = n_{p0}\, \mathrm{e}^{-\nu\xi/c}[H(\xi) - H(\xi - c\tau)], \tag{2.5}$$

$$\begin{aligned} n_b(\xi, \tau) = \frac{n_{p0}}{1 - \beta_x}[&(1 - \mathrm{e}^{-\nu\xi/c})H(\xi) \\ &+ (\mathrm{e}^{-(\nu/v_x)(\xi - c\tau(1-\beta_x))} - 1)H(\xi - c\tau(1 - \beta_x))]. \end{aligned} \tag{2.6}$$

The normalized beam velocity β_x can be estimated as $\beta_x \simeq \sqrt{\langle \beta_x^2 \rangle_\Omega}$. In the high-energy limit $\epsilon \gg 1$, $\beta_x \simeq 1 - 1/(2\epsilon \ln \epsilon)$. For large times $t \gg 1/[\nu(1 - \beta_x)]$, (2.6) implies that the beam cannot exceed the maximum density $n_{p0}/(1 - \beta_x) \simeq 2n_{p0}\epsilon \log \epsilon$. Because we expect collective processes for such time scales, we underline that this limit is unlikely to be reached and should be considered as an upper bound of the maximum achievable density. This maximum density could however be achieved in cases where collective effects are damped on large distances, for example, either with a high magnetic field oriented in the flow direction or a large background plasma temperature.

To clarify some of the properties of this solution, we recast it with (x, t) variables and in the limits $\nu t \ll 1$ and $\beta_x \simeq 1$ and therefore get, for all $0 \leq x \leq ct$,

$$n_p(x, t) = n_{p0}(1 + \nu x/c - \nu t), \tag{2.7}$$

$$n_b(x, t) = n_{p0}\nu x/c. \tag{2.8}$$

The result in (2.7) illustrates that the background plasma density evolves linearly with the position $x = 0 \to ct$, increasing from $n_{p0}(1 - \nu t)$ to its maximum value n_{p0}. Equation (2.8) clarifies that the beam density is expected to grow linearly with the propagation distance, starting from 0 and increasing to its maximum value $n_{p0}\nu t$ at the position of the photon front $x = ct$.

We stress this model is valid whatever the photon and plasma densities. It remains applicable as long as collective plasma effects do not play a significant role. In terms of photon energies, the model is strictly limited to the range $1 \ll \epsilon < 1/\alpha_f = 137$. However, we will discuss in § 4 why it can be extended to a larger range of $20 \lesssim \epsilon \lesssim 200$. To account for photons in the energy range $1 \lesssim \epsilon \lesssim 20$, one would need to account for the much larger energy spread induced by the Compton cross-section and also to include the two-photon Breit–Wheeler pair creation.

https://doi.org/10.1017/S0022377821000660 Published online by Cambridge University Press

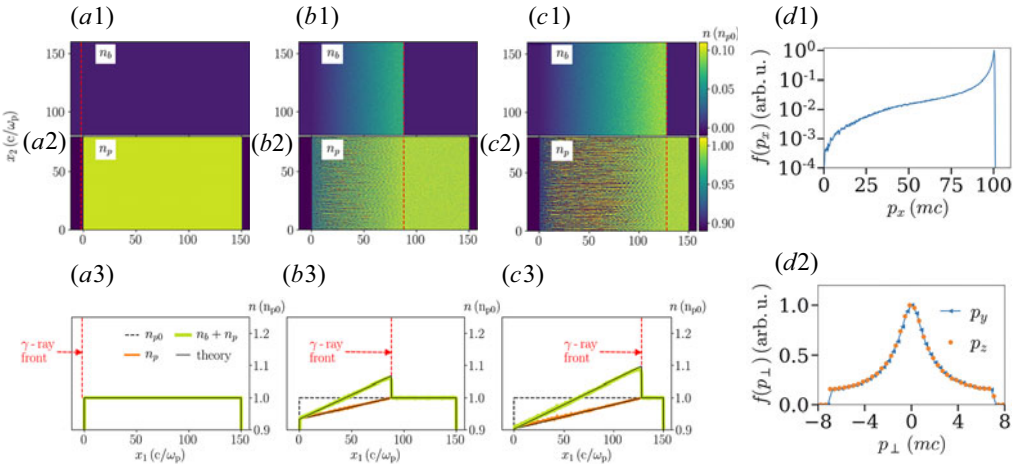

FIGURE 1. (*a*1,*b*1,*c*1) The two-dimensional (2-D) electron beam density profile at three instants: (*a*1) $\omega_p t = 0$; (*b*1) $\omega_p t = 90$; and (*c*1) $\omega_p t = 130$. (*a*2,*b*2,*c*2) The 2-D electron background density profile for the same three instants. (*a*3,*b*3,*c*3) One-dimensional projections along propagation direction x for the same instants. The orange curve is the background plasma density n_p, the green thick curve is the total density $n_p + n_b$ and the black curves are the theoretical estimates from (2.5) and (2.6). The gamma-ray beam propagates from left to right and its front is marked by the dashed red line. (*d*1,*d*2) $f(p_x)$ and $f(p_\perp)$ Distributions of electrons scattered by Compton at the beam front for time $\omega_p t = 130$. For the plasma density $n_{p0} = 1\ \mathrm{cm}^{-3}$, one has $c/\omega_p = 5.3 \times 10^5$ cm.

We have reported how a pair beam can be created when gamma rays propagate in a background pair plasma via Compton scattering. This process is corroborated by theory and is now confronted to simulation results. We have run 2-D PIC simulations with OSIRIS (Fonseca *et al.* 2002). These simulations were recently enriched with a Compton scattering module (Del Gaudio *et al.* 2020*b*), similar to earlier work (Haugbølle, Frederiksen & Nordlund 2013). The simulation proceeds through two key steps: first a random pairing of macro particles at every time step and in every cell and second a Monte Carlo sampling of the angle-resolved Klein–Nishina cross-section (Klein & Nishina 1928). For every binary collisions treated, the cross-section is evaluated in the electron rest-frame, an energy and momentum balance is ensured, and a splitting technique is employed to handle the varying weight of macro particles. This implementation relies on macro particle pairing and therefore stands out from other works (Levinson & Cerutti 2018) where the Compton cross-section is evaluated from the intensity of the ambient radiation field.

We detail the relativistic pair beam formation from an illustrative simulation in figure 1. We consider a cold pair plasma (1 eV) with a uniform density $n_{p0} = 1\ \mathrm{cm}^{-3}$, as displayed in figure 1(*a*1–*a*3). In this pair plasma, we propagate a monoenergetic ($\epsilon = 100$) gamma-ray beam along the x direction from left to right. This presents a uniform density $n_{\omega 0} = 10^{17}\ \mathrm{cm}^{-3}$ with a front indicated by the red dashed line in figure 1(*a*3,*b*3,*c*3). Periodic boundary conditions are assumed in the transverse direction y for all species and fields, and open boundary conditions are employed in the longitudinal x direction. The domain extends to $(160c/\omega_p)^2$ with 2000^2 cells. The cell dimensions are $\delta x = \delta y = 0.08c/\omega_p$ and the time step is $\delta t = \delta x/2$. We initialize 80/80/160 particles per cell for electrons, positrons and photons.

The process of pair beam formation is illustrated in figure 1. Figure 1(*a*1,*b*1,*c*1) exhibit 2-D profiles of the electron beam density n_b at three instants $\omega_p t = 0$, 90 and 130.

https://doi.org/10.1017/S0022377821000660 Published online by Cambridge University Press

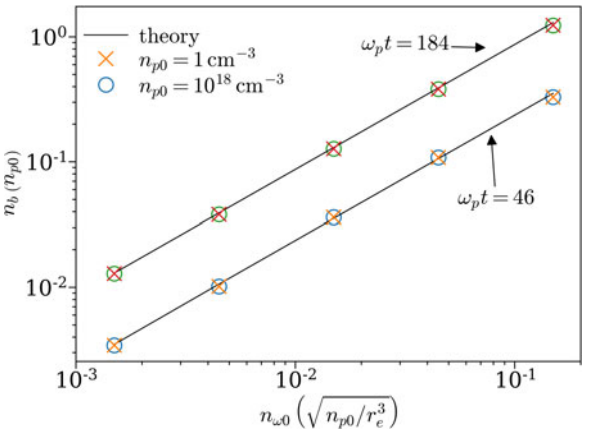

FIGURE 2. Pair beam density n_b/n_{p0} versus the photon density $n_{\omega 0}$ in units of $\sqrt{n_{p0}/r_e^3}$ for plasma densities $n_{p0} = 1\ \mathrm{cm}^{-3}$ (X) and $n_{p0} = 10^{18}\ \mathrm{cm}^{-3}$ (O) at two times in the simulations. The plasma angular frequency is ω_p.

The profiles correspond to electrons which experienced at least one Compton scattering. Figure 1(*a*2,*b*2,*c*2) represent 2-D profiles of the electron background density n_p for the same three instants $\omega_p t = 0$, 90 and 130. Figure 1(*a*3,*b*3,*c*3) shows the averages of theses 2-D densities along y the transverse direction. To clarify the plot, only the total density $n_b + n_p$ (green thick curve) and background density n_p (orange thin curve) are represented. Based on these figures, we can observe the formation and propagation of an electron beam (positrons are superimposed by symmetry). We found excellent agreement of the simulations with the theoretical estimates (black lines) of (2.5) and (2.6). The simulation times considered here ($\omega_p t \leq 130$) lie within the limit $vt \ll 1$ where we derived (2.7) and (2.8). For such early times, the beam and background densities have profiles increasing linearly with the propagation distance, which explains the triangular shape of the total density profile in figure 1(*b*3,*c*3). The momenta distributions $f(p_x)$ and $f(p_\perp)$ of deflected electrons are exemplified in figure 1(*d*1,*d*2) at time $\omega_p t = 130$. The distribution $f(p_x)$ exposes a peak at $p_x/mc \simeq 100 = \epsilon$, exactly as our theoretical estimate in (2.1*a*,*b*). The transverse momentum profile $f(p_\perp)$ includes both directions p_y and p_z. The two distributions are centred and characterized by a $\simeq 3mc$ standard deviation, in agreement with (2.1*a*,*b*). This is conducted in the range of validity of the theoretical model with periodic conditions in the transverse direction, and does not provide evidence for collective plasma processes with a significant impact on the beam formation.

Another set of 2-D simulations was run to assert the relevance of this process of beam formation. Our goal is to check the range of validity of the scaling inferred for its peak density in (2.6). We consider two sets of simulations. The first set is characterized by a pair plasma of density $n_{p0} = 10^{18}\ \mathrm{cm}^{-3}$, with photon densities $n_{\omega 0} = 10^{25}$–$10^{27}\ \mathrm{cm}^{-3}$. The second presents a pair plasma density of $n_{p0} = 1\ \mathrm{cm}^{-3}$, with photon densities $n_{\omega 0} = 10^{16}$–$10^{18}\ \mathrm{cm}^{-3}$. Connections of these parameters to laboratory or astrophysical parameters will be discussed in § 5. Given the symmetry of our problem, we reduce the domain size to $(24c/\omega_p)^2$ and follow the photon beam in a moving window with a velocity equal to c. The domain has 600^2 cells with dimensions $\delta x = \delta y = 0.04c/\omega_p$ and a time step $\delta t = \delta x/2$.

Figure 2 represents the pair beam density as a function of the incident photon density for two instants, $\omega_p t = 46$ and 184. The normalization by the quantity $(n_{p0}/r_e^3)^{1/2}$ comes from a factor v/ω_p in (2.8). This reveals a general scaling of the normalized pair beam

https://doi.org/10.1017/S0022377821000660 Published online by Cambridge University Press

density n_b/n_{p0}, independent of the initial plasma density n_{p0}. Despite such a wide gap of initial plasma densities considered in figure 2, simulations clarify that the normalized pair beam density at a given time t remains exactly the same as long as $n_{\omega 0}(r_e^3/n_{p0})^{1/2}$ (or ν/ω_p) is constant. This scaling matches exactly with the prediction of (2.6), illustrated as a black line in figure 2.

We have generalized the validity of the results obtained in figure 2 to account for baryon loading in the background plasma. First, we ran all the simulations presented before with a fraction f of proton density up to $f = 0.1n_{p0}$ in the pair plasma. As the initial electron and positron plasma densities are not equal, the beam driven by Compton now presents a non-uniform charge and current densities. This initiates the start of the two-stream instability. The growth rate of such instability is much lower than the oblique instability (Bret, Firpo & Deutsch 2005*b*) by a factor $\gamma_b^{2/3}$, with γ_b as the Lorentz factor of the beam. As a consequence, the exponential growth of the oblique modes we report in the next section still takes place, but is initiated in a slightly perturbed plasma. Second, we ran one three-dimensional (3-D) simulation, which confirmed our previous findings. We performed the simulation for a plasma density of $n_{p0} = 1$ cm^{-3} and photon density of $n_{\omega 0} = 10^{18}$ cm^{-3}. The domain size was $(24c/\omega_p)^3$ and the photon beam was followed in a moving window with a velocity equal to c. The domain had 600^3 cells of dimensions $\delta x = \delta y = \delta z = 0.04c/\omega_p$ and the time step was $\delta t = \delta x/2$. We initialized 2/2/4 particles per cell for electrons, positrons and photons. The transverse boundary conditions for particles and fields were all periodic. For this 3-D simulation (not shown here), the evolution of the peak beam density was the same as for the 2-D simulation with the same parameters. While we will discuss this in detail in § 3, we add that the growth rate of the beam plasma instability in this 3-D simulation is also the same as in the corresponding 2-D simulation.

3. Onset of a beam-plasma instability

The normalized pair beam density n_b/n_{p0} increases with time and is expected to trigger an electromagnetic beam-plasma instability when $n_b/n_{p0} \lesssim 1$. Two types of modes can compete and lead to an exponential growth of magnetic fields (Bret, Firpo & Deutsch 2005*a*). The first type is the modes associated to the current filamentation instability (CFI), with growth rate $\omega_p^{-1}\Gamma_{\rm CFI} = (n_b/n_{p0}\gamma_b)^{1/2}$. The second type is the modes corresponding to the oblique filamentation instability (OBI), with growth rate $\omega_p^{-1}\Gamma_{\rm OBI} = \sqrt{3}(n_b/n_{p0}\gamma_b)^{1/3}/2^{4/3}$. We can predict that our prevailing modes will be oblique because we consider Lorentz factors $1 \ll \gamma_b \lesssim 1/\alpha_f$ and densities $n_b/n_{p0} \leq 1$. Above some critical angle in $\boldsymbol{k}$ space, such modes are expected to be damped like CFI modes arising from thermal effects (Bret *et al.* 2005*a*). The physical reason is that a transverse thermal expansion of filaments competes with the magnetic pinching force maintaining them (Silva *et al.* 2002). The latter theoretical work provides a density threshold above which the instability can still be set off despite this initial spread. It reads $\alpha_{\rm th} = n_b/n_{p0} \simeq \gamma_b(p_\perp/mc\gamma_b)^2$. Using the estimates from (2.1*a*,*b*), we get $n_b/n_{p0} \simeq 7/(6\ln\epsilon)$ and

$$\omega_p^{-1}\Gamma \simeq (7\sqrt{3}/16)^{1/3}[\epsilon\log(\epsilon)]^{-1/3}. \tag{3.1}$$

The minimum density required to trigger the instability is reached after a propagation time of $1/(\nu\ln\epsilon)$. Using (2.6), this implies the photons should propagate through a plasma of length greater than $r_{\rm min} \geq c/(\nu\ln\epsilon)$. This condition can be recasted as

$$r_{\rm min}[{\rm cm}] \geq 1.6\times 10^{25} n_\omega^{-1}[{\rm cm}^{-3}]. \tag{3.2}$$

https://doi.org/10.1017/S0022377821000660 Published online by Cambridge University Press

The beam density threshold $\alpha_{\rm th} = 6/(7\ln\epsilon)$ is independent from the initial plasma density, and so is the plasma length $r_{\rm min}$ given in (3.2). It is worthwhile to stress that provided the photon density and the background plasma length satisfy the condition in (3.2), the instability will take place. As far as the effect of the background plasma temperature is concerned, we can rely on previous investigations (Bret *et al.* 2005*b*). For the non-relativistic background plasma temperature considered here (1 eV), we do not expect any mitigation effect on the onset of CFI-like modes.

In addition, it seems meaningful to evaluate the energy conversion efficiency from the incident photons to magnetic fields. We define $\eta = \mathcal{E}_{B_z}/\mathcal{E}_{\omega 0}$, the ratio between the magnetic energy $\mathcal{E}_{B_z} \simeq \int c^2 B_z^2/8\pi \, {\rm d}\boldsymbol{x}$ and the incident photon energy. For a semi-infinite beam (and 1-D), the ratio η is also the ratio of the energy densities. For the sake of simplicity, we estimate an upper bound for the magnetic field energy $\mathcal{E}_{B_z} \lesssim \int c^2|B_z|^2/8\pi \, {\rm d}\boldsymbol{x}$. Using Parseval theorem, this can be expressed as $\mathcal{E}_{B_z} \lesssim \int c^2|B_z|^2/8\pi \, {\rm d}\boldsymbol{k}$. The value of the saturated magnetic field can be approximated by equating the bounce frequency of trapped particles to the growth rate of the instability (Yang, Arons & Langdon 1994). This maximum is $eB_z(k)/m\omega_p \simeq (\gamma_b^2/p_x)(\omega_p^{-1}\Gamma)^2\omega_p/kc$. The energy conversion efficiency is then deduced by introducing the incident photon energy density $\epsilon n_{\omega 0}$

$$\eta \lesssim \frac{1}{4\pi}\left(\frac{7\sqrt{3}}{16}\right)^{4/3}\frac{n_{p0}}{n_{\omega 0}}\frac{1}{(\epsilon\ln^4(\epsilon))^{1/3}}. \tag{3.3}$$

It is important to underline that this inequality only expresses an upper bound for the conversion efficiency. For any given plasma of density n_{p0}, (3.3) predicts that η can be maximized for smaller incident photon densities $n_{\omega 0}$. However, decreasing the photon density limits the growth of the beam density through Compton scattering and therefore increases the propagation distance required to trigger the instability, as evidenced in (3.2). As a consequence of this low conversion efficiency η, the generation of magnetic fields can, in principle, take place over long distances. For a perfectly collimated photon source emerging from the photosphere ($\simeq 10^{12}$ cm), this length can be as high as the Compton mean free path L_ω [cm] $= c\tau_\omega \simeq 10^{25} n_{p0}^{-1}$ [cm^{-3}]. In fact, the typical opening angle of the GRB ejecta is in the range $\theta \leq 20^\circ$, as estimated by Racusin *et al.* (2009). With this more realistic assumption, the photon density and the beam density are expected to decrease with the propagation distance as $1/r^2$ owing to this transverse dilution effect. We estimate under which condition this depletion of the beam may remain negligible compared with the loading via Compton scattering as

$$\frac{\nu}{c}(r - r_{\rm ph})\left(\frac{r_{\rm ph}}{r}\right)^2 \geq 1 \rightarrow r \leq \sigma_{\rm kn} n_{\omega 0} r_{\rm ph}^2 = r_{\rm max}. \tag{3.4}$$

The inequality (3.4) states that the density increase owing to the Compton loading between $r_{\rm ph}$ and r is $\nu(r - r_{\rm ph})/c$ and remains larger than the density decrease between $r_{\rm ph}$ and r owing to the transverse dilution, which is $(r_{\rm ph}/r)^2$. The inequality (3.4) provides a maximum distance, denoted as $r_{\rm max}$, over which the instability can be sustained.

Given a gamma-ray density between 10^{14} cm^{-3} and 10^{22} cm^{-3} that we inferred at the exit of the photosphere of GRBs (see § 5), the condition (3.4) is fulfilled for distances ranging from a few photospheric radii $\sim 10^{12}$ cm up to larger values of 10^{20} cm. We did not verify this estimate in simulations owing to the computational cost for very long propagation lengths L [cm] $\geq 10^8 n_{p0}^{-1/2}$ [cm^{-3}].

https://doi.org/10.1017/S0022377821000660 Published online by Cambridge University Press

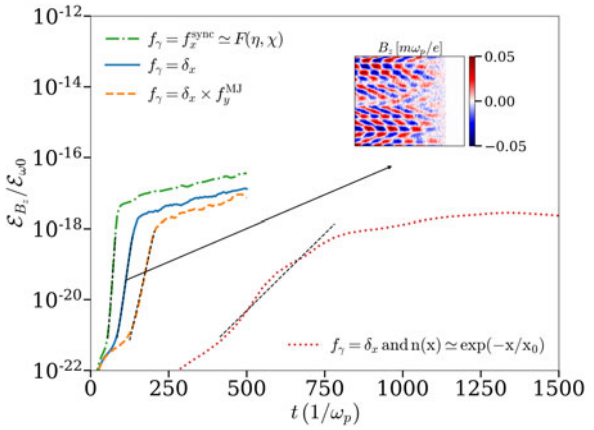

FIGURE 3. Magnetic field energy $\mathcal{E}_{B_z}$, normalized by the incident photon energy $\mathcal{E}_{\omega 0}$. We denote $\eta = \mathcal{E}_{B_z}/\mathcal{E}_{\omega 0}$ and derive an upper bound in (3.3). Simulation for a monoenergetic photon distribution (blue solid curve), a Maxwell–Jüttner transverse profile (orange dashed curve), a front density gradient (red dotted curve) and a synchrotron distribution (green dash–dotted curve). The growth rate of the field is determined from the slope of the black dashed curves. Inset: typical B_z field profile during the linear phase.

4. Generalization for various photon distributions

In the previous section, we have considered idealized photon distributions. We now examine more realistic photon distribution functions.

We investigate a simulation with plasma density $n_{p0} = 10^8$ cm^{-3} and photon density $n_{\omega 0} = 10^{22}$ cm^{-3}. We employ the δ notation for a Dirac delta function, and can write the momentum distribution of the photons as $f = f_x = \delta(p_x - 100mc)$. Figure 3 reports the energy of the B_z field, denoted by $\mathcal{E}_{B_z}$ and normalized by the incident photon energy $\mathcal{E}_{\omega 0}$ (blue solid curve). We first focus on the monoenergetic photon distribution (blue solid curve). The growth rate for all modes $\boldsymbol{k}$ is $\omega_p^{-1}\Gamma = 7.4 \times 10^{-2}$. The B_z field profile is displayed during the linear phase of the instability (see the inset) and shows that the dominant mode is oblique: $\boldsymbol{k} = (k_x, k_y) \simeq (1.8, 1.4)\omega_p/c$. Its growth rate is $\omega_p^{-1}\Gamma = 0.12$ close to $\omega_p^{-1}\Gamma \simeq 0.118$, which is the theoretical prediction from (3.1). The linear stage of the instability starts after a propagation distance $\simeq 90c/\omega_p$, which is consistent with the minimum inferred theoretically of $34c/\omega_p$ in (3.2). The theoretical upper bound of the energy conversion efficiency given by (3.3) is $\eta \lesssim 1.5 \times 10^{-17}$, which is of the order of the simulation result $\eta = 5 \times 10^{-18}$. We also checked that the pair beam density rises slowly (+30 %) on the instability time scale for $\omega_p t = 90$–150. This legitimates *a posteriori* the use of estimates from linear theory. However, during the saturation stage, for $\omega_p t = 150$–500, the front beam density increases from n_{p0} up to $\sim 4n_{p0}$, a value which is in agreement with that from (2.8). As a consequence, the beam keeps on filamenting and the magnetic field energy keeps increasing.

The aforementioned discussions are focused on a monoenergetic gamma-ray beam. We intend to extend these results for more complex distributions. First, we consider a photon distribution $f = f_x f_y$ with $f_x = \delta(p_x - 100mc)$ and f_y a Maxwell–Jüttner distribution of temperature $T_{\gamma,\perp}$. In the case where $T_{\gamma,\perp}/mc^2 \ll \Delta p_\perp/mc$, with $\Delta p_\perp/mc = \sqrt{7\epsilon/(6\ln\epsilon)}$ given by (2.1*a*,*b*), the results we have discussed before are not changed because the transverse momentum spread of the beam only arises from the Compton scattering kinematics. In the other limit $T_{\gamma,\perp}/mc^2 \gtrsim \sqrt{7\epsilon/(6\ln\epsilon)}$, the transverse momentum spread

https://doi.org/10.1017/S0022377821000660 Published online by Cambridge University Press

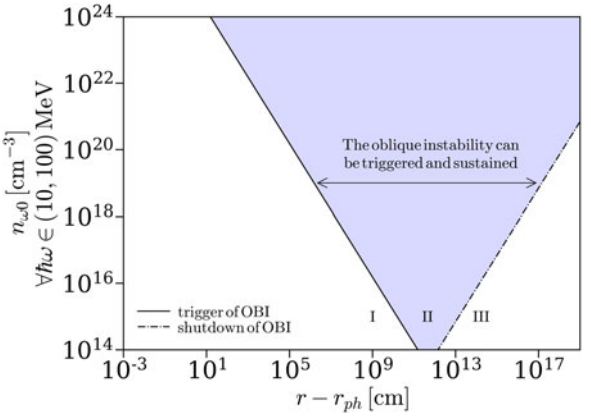

FIGURE 4. Relevance of the pair beam formation and magnetization in the frame of the GRB–CBM interaction at the photospheric radius $r_{\mathrm{ph}} \sim 10^{12}$ cm. On the left side of the continuous line (area I): one expects only pair beam formation. Between the continuous and dash–dotted lines (area II), one also expects the beam-plasma instability. On the right side of the dash–dotted (area III), the instability is shutdown owing to the transverse dilution of the beam.

of the beam is determined by $T_{\gamma,\perp}$. Because the Compton cross-section is beamed for gamma rays, the pair beam presents a similar transverse momentum spread as the photon beam, which is known to lower the growth rate of the OBI (Bret, Gremillet & Bénisti 2010). The latter behaviour is confirmed in figure 3 where we choose $T_{\gamma,\perp} = 3mc^2$. This implies a transverse momentum spread of $\Delta p_\perp/mc = 6$ for the photon source, while the Compton-induced spread is $\Delta p_\perp/mc = \sqrt{7\epsilon/(6\ln\epsilon)} = 5$. As expected, this leads to a reduction of the growth rate $\omega_p^{-1}\Gamma = 7.4 \times 10^{-2} \to 4.5 \times 10^{-2}$, see the orange dashed curve. Second, we consider that the photons have a monoenergetic distribution $f = f_x$ with $f_x = \delta(p_x - 100mc)$ but their density profile has an exponential shape $\propto \exp(-x/100)$ of scale length $100c/\omega_p$, followed by a flat profile of density $n_{\omega 0}$. Because the pair beam density is proportional to the photon density, its profile first presents a density gradient and then the triangular shape, as observed in figure 1(*b*3,*c*3). As a result, the growth of the OBI is delayed in time, and is slightly lower but noticeable ($\omega_p^{-1}\Gamma \simeq 1.0 \times 10^{-2}$). This time delay is comparable to the gradient length, as can be seen by the red dotted curve in figure 3. Third, we model a synchrotron distribution for the incident photon beam. We set up this energy distribution as a longitudinal momentum distribution for the photons $f = f_x = F(\eta, \chi)$ (Klepikov 1954). The function F represents the synchrotron spectra of an electron with a quantum parameter η, χ being the photon quantum parameter. It has a peak at an energy of $\hbar\omega/mc^2 = 100$. Photons with an energy of 10–100 MeV are Compton scattered and contribute to increase the pair beam density compared with the monoenergetic case. Indeed, the Klein–Nishina cross-section is a decreasing function of photon energy. As a result, the growth of the B_z field energy is faster: $\omega_p^{-1}\Gamma = 7.4 \times 10^{-2} \to 1.2 \times 10^{-1}$, as seen by the green dash–dotted curve in figure 3.

5. Relevance for astrophysics and laboratory environments

We now discuss under which conditions this process can be observed in astrophysics and in the laboratory.

Figure 4 covers a large range of photon densities $n_{\omega 0}$ and distances $r - r_{\mathrm{ph}}$, with r_{ph} the photospheric radius of a GRB. It reports whether the propagation distance is large enough to enable the instability to be triggered, see (3.2). The latter limit is plotted by the

https://doi.org/10.1017/S0022377821000660 Published online by Cambridge University Press

continuous line in figure 4 and enables the distinction of two regimes of interaction. The first interaction regime is represented by all the area on the left side of the continuous line and is denoted as I. In this case, the photons are expected to form a relativistic electron positron beam via Compton scattering. However, the pair beam density is too low and its transverse momentum spread is too high to enable the onset of the instability, as detailed in § 3. The second interaction regime is depicted by the area between the continuous and dash–dotted lines and is denoted as II. In this regime, the pair beam density grows high enough to allow the instability to develop. The dash–dotted line illustrates the maximum length of the filament, as estimated in (3.4). This corresponds to the radius above which the beam density is depleted by dilution effects faster than it is loaded via Compton scattering.

For the photospheric radius of a GRB, we evaluated a range of relevant gamma-ray densities. With estimates from the fireball model, this gamma-ray density (10–100 MeV) is determined to be $n_\omega \in (10^{14}, 10^{22})$ cm^{-3}. From this order of magnitude, we observe in figure 4 that such conditions can trigger the instability and its development at large distances. To be more precise, the instability can be expected for GRBs whenever their gamma-ray density at the photosphere radius is above 10^{14} cm^{-3}, which corresponds to a GRB with an isotropic equivalent luminosity above 3×10^{50} erg s^{-1}. The second important result is that the beam density remains high enough to sustain the instability at large distances, despite its transverse dilution. For example, the instability can be maintained at distances $\geq 10^{17}$ cm for gamma-ray densities $\geq 10^{19}$ cm^{-3}, and this corresponds to an isotropic equivalent luminosity $\geq 10^{52}$ erg s^{-1}.

We now detail the estimates to infer what is the gamma-ray density at the photosphere radius, following Kumar & Zhang (2015). Let us consider a compact object with a radius $\sim 10^7$ cm and an isotropic equivalent luminosity $\mathcal{L}$ in erg s^{-1}. For simplicity we provide the estimate in the compact object frame, thus neglecting the red shift of its host galaxy. The fireball emerges from the compact object and experiences an adiabatic expansion. At the photospheric radius $\sim 10^{12}$ cm, the emergent thermal radiation from the photosphere has a luminosity which is equivalent to a blackbody temperature of [1.3 MeV] $\times \mathcal{L}_{52}^{1/4}$. The notation $\mathcal{L}_{52}$ is defined as $\mathcal{L}_{52} = \mathcal{L}/(10^{52}$ erg s). We assume typical GRBs have an isotropic equivalent luminosity in the range $\mathcal{L} \in (10^{47}$–$10^{54})$ erg s^{-1}, in line with data recently gathered (Abbott *et al.* 2017). This leads to the conclusion that this blackbody equivalent temperature for the luminosity at the photospheric radius ranges from 70 keV up to 4 MeV. However, the isotropic equivalent luminosity is defined for photons in the standard energy band 1 keV up to 10 MeV. We then deduce the fraction of photons in the energy range 10–100 MeV, where our results are valid, by assuming a black body energy distribution. For instance, this ratio of photons (10–100 MeV) becomes $\gtrsim 5$ % if the GRB isotropic equivalent luminosity is $\gtrsim 10^{52}$ erg s^{-1}. The final step is to deduce a gamma-ray density from this total luminosity in gamma rays. To this purpose, we assumed the GRB ejecta is a spherically expanding shell and its thickness is the GRB duration, typically ranging between 0.1 and 100 s.

We now discuss the role of an external magnetic field that can be expected in an astrophysical scenario. It is expected that an external and strong enough magnetic field aligned with the flow will prevent the development of the current filamentation instability (Molvig 1975). It was however demonstrated that if the field is not strictly aligned with the flow, then the instability is ensured to take place with a reduced growth rate for a non-relativistic beam temperature (Bret & Alvaro 2011). This growth rate is a fraction of the growth rate without any magnetic field. Its detailed value in the low- and high-magnetization limits can be found in (8) and (10) of the paper by Bret & Alvaro (2011).

https://doi.org/10.1017/S0022377821000660 Published online by Cambridge University Press

It is worth questioning whether this Compton-driven beam formation and magnetization can take place in the laboratory. Despite the ongoing worldwide efforts, no large size and confined pair plasmas have been formed in a laboratory environment yet. One can still mention that pair jets of high density $n_{p0} \sim 10^{16}$ cm^{-3} can be generated by fast electrons going through mm-sized high-Z targets. The fast electrons can be generated by an intense laser (Chen *et al.* 2015; Liang *et al.* 2015) or by a plasma wakefield accelerator (Sarri *et al.* 2015; Xu *et al.* 2016). Recent numerical work has brought forward a new scheme to create dense pair jets $n_{p0} \sim 10^{13}$ cm^{-3} with size of several skin-depths in all directions from the interaction of relativistic protons (400 GeV c^{-1}) with a solid beryllium/lead target (Arrowsmith *et al.* 2020). Regarding gamma-ray sources (10–100 MeV), we estimated a density $n_{\omega 0} \sim 10^{17}$ cm^{-3} for the experimental photon source recently obtained by nonlinear inverse Compton scattering (Cole *et al.* 2018; Poder *et al.* 2018). For such a photon density, one would need a plasma length of 10^8 cm to witness the instability, which cannot be achieved in a laboratory environment. We also consider the results of a recent simulation from an extremely dense gamma-ray source obtained during the interaction of a dense electron beam with multiple micron-sized foils (Sampath *et al.* 2021). Although it remains a numerical result and its experimental realization may lie far in the future, it achieves a record gamma-ray density of $n_{\omega 0} \sim 10^{23}$ cm^{-3} with a distribution peaked at 100 MeV. One can see in figure 4 that even this high gamma-ray density might be enough to witness the onset of the Compton-driven instability in a laboratory frame. One would need a plasma length of 150 cm to observe it. Overall, our results indicate that exploration of the process of beam formation and magnetization in the laboratory is unlikely in the short term owing to the combined requirements of plasma length and gamma-ray densities.

6. Conclusions

To summarize, we reported a study of gamma-ray propagation in a background pair plasma. We showed that it can lead to the formation of a relativistic pair beam, thanks to the beaming of the Compton cross-section for photons above 10 MeV. A theoretical model to describe the formation of the beam driven by Compton scattering has been developed, and compared with PIC simulations. We showed the pair beam can achieve a relativistic Lorentz factor with a density comparable to the background plasma. In addition, we quantified the transverse momentum spread of the beam, which is induced by the Compton cross-section. We demonstrated that the pair beam, as it propagates, can convert its kinetic energy to magnetic energy via the oblique instability, although limited by its transverse momentum spread. The conversion efficiency of this process is low, but it can occur over long distances. We extrapolated from PIC simulations that it could lead to the generation of magnetic fields on distances larger than a parsec (up to $\simeq 10^{25}$ cm) for a perfectly collimated GRB ejecta. For a less collimated one ($\theta \leq 20^\circ$), we estimated the instability can be sustained over long distances $10^{12} \rightarrow 10^{17}$ cm for GRBs with an isotropic equivalent luminosity ranging from 3×10^{50} to 10^{52} erg s^{-1}. We showed that these results can be used to address the energy dissipation of gamma rays at the photospheric radius of GRBs. We checked the robustness of our results for various types of photon sources, with non-uniform density profiles and transverse and longitudinal spreads in their momentum distribution. The simulations done in the frame of this study are performed for the typical orders of magnitude for plasma and photon densities expected at the photospheric radius of a GRB, using estimates from the hot fireball model as well as data recently gathered on GRBs.

This work offers two directions to explore in the future. The first could be to consider photon distributions with energies below 10 MeV to connect with previous works on

https://doi.org/10.1017/S0022377821000660 Published online by Cambridge University Press

Compton-driven plasma wakes (Frederiksen 2008; Del Gaudio *et al.* 2020*a*). The second is to understand the impact of the beam formation and magnetization on global GRB models.

Acknowledgements

The authors acknowledge fruitful discussions with Drs Del Gaudio and Schoeffler.

Editor Antoine C Bret thanks the referees for their advice in evaluating this article.

Funding

This work was supported by the European Research Council (ERC-2015-AdG Grant 695088). We also acknowledge PRACE for awarding access to MareNostrum based in Spain.

Declaration of interests

The authors report no conflict of interest.

REFERENCES

ABBOTT, B.P., ABBOTT, R., ABBOTT, T.D., ACERNESE, F., ACKLEY, K., ADAMS, C., ADAMS, T., ADDESSO, P., ADHIKARI, R.X., ADYA, V.B. & LIGO VIRGO COLLABORATION 2017 Gravitational waves and gamma rays from a binary neutron star merger: GW170817 and GRB 170817a. *Astrophys. J.* **848** (2), L13.

ACCIARI, V.A., ANSOLDI, S., ANTONELLI, L.A., ENGELS, A.A., BAACK, D., BABIĆ, A., BANERJEE, B., BARRES DE ALMEIDA, U., BARRIO, J.A., GONZÁLEZ, J.B. & MAGIC COLLABORATION 2019 Observation of inverse compton emission from a long γ-ray burst. *Nature* **575** (7783), 459–463.

ARROWSMITH, C.D., SHUKLA, N., CHARITONIDIS, N., BONI, R., CHEN, H., DAVENNE, T., FROULA, D.H., HUFFMAN, B.T., KADI, Y., REVILLE, B., RICHARDSON, S., SARKAR, S., SHAW, J.L., SILVA, L.O., TRINES, R.M.G.M., BINGHAM, R. & GREGORI, G. 2020 Generating ultra-dense pair beams using 400 gev/c protons. *Phys. Rev. Research* **3**, 023103.

BELOBORODOV, A.M. 2005 Afterglow emission from pair-loaded blast waves in gamma ray bursts. *Astrophys. J.* **627** (1), 346–367.

BLUMENTHAL, G.R. & GOULD, R.J. 1970 Bremsstrahlung, synchrotron radiation, and compton scattering of high energy electrons traversing dilute gases. *Rev. Mod. Phys.* **42**, 237–270.

BRET, A. & ALVARO, E.P. 2011 Robustness of the filamentation instability as shock mediator in arbitrarily oriented magnetic field. *Phys. Plasmas* **18** (8), 080706.

BRET, A., FIRPO, M.-C. & DEUTSCH, C. 2005*a* Characterization of the initial filamentation of a relativistic electron beam passing through a plasma. *Phys. Rev. Lett.* **94**, 115002.

BRET, A., FIRPO, M.-C. & DEUTSCH, C. 2005*b* Electromagnetic instabilities for relativistic beam-plasma interaction in whole k space: nonrelativistic beam and plasma temperature effects. *Phys. Rev.* E **72**, 016403.

BRET, A., GREMILLET, L. & BÉNISTI, D. 2010 Exact relativistic kinetic theory of the full unstable spectrum of an electron-beam–plasma system with Maxwell-Jüttner distribution functions. *Phys. Rev.* E **81**, 036402.

CAVALLO, G. & REES, M.J. 1978 A qualitative study of cosmic fireballs and gamma ray bursts. *Mon. Not. R. Astron. Soc.* **183** (3), 359–365.

CHEN, H., LINK, A., SENTOKU, Y., AUDEBERT, P., FIUZA, F., HAZI, A., HEETER, R.F., HILL, M., HOBBS, L., KEMP, A.J., KEMP, G.E., KERR, S., MEYERHOFER, D.D., MYATT, J., NAGEL, S.R., PARK, J., TOMMASINI, R. & WILLIAMS, G.J. 2015 The scaling of electron and positron generation in intense laser-solid interactions. *Phys. Plasmas* **22** (5), 056705.

COLE, J.M., *et al.* 2018 Experimental evidence of radiation reaction in the collision of a high-intensity laser pulse with a Laser-Wakefield accelerated electron beam. *Phys. Rev.* X **8**, 011020.

https://doi.org/10.1017/S0022377821000660 Published online by Cambridge University Press

Del Gaudio, F., Fonseca, R.A., Silva, L.O. & Grismayer, T. 2020*a* Plasma wakes driven by photon bursts via compton scattering. *Phys. Rev. Lett*. **125**, 265001.

Del Gaudio, F., Grismayer, T., Fonseca, R.A. & Silva, L.O. 2020*b* Compton scattering in particle-in-cell codes. *J. Plasma Phys*. **86** (5), 905860516.

Fonseca, R.A., Silva, L.O., Tsung, F.S., Decyk, V.K., Lu, W., Ren, C., Mori, W.B., Deng, S., Lee, S., Katsouleas, T. & Adam, J.C. 2002 Osiris: a three-dimensional, fully relativistic particle in cell code for modeling plasma based accelerators. In *Computational Science — ICCS 2002* (ed. P. M. A. Sloot, A. G. Hoekstra, C. J. Kenneth Tan & J. J. Dongarra), pp. 342–351. Springer.

Frederiksen, J.T. 2008 Stochastically induced gamma ray burst wakefield processes. *Astrophys. J*. **680** (1), L5–L8.

Gruzinov, A. & Mészáros, P. 2000 Photon acceleration in variable ultrarelativistic outflows and high-energy spectra of gamma ray bursts. *Astrophys. J*. **539** (1), L21–L24.

Haugbølle, T., Frederiksen, J.T. & Nordlund, Å. 2013 photon-plasma: a modern high-order particle-in-cell code. *Phys. Plasmas* **20** (6), 062904.

Klein, O. & Nishina, Y. 1928 The scattering of light by free electrons according to Dirac's new relativistic dynamics. *Nature* **122** (3072), 398–399.

Klepikov, N.P. 1954 Emission of photons or electron-positron pairs in magnetic fields. *J. Exp. Theor. Phys*. **26**, 19.

Kumar, P. & Zhang, B. 2015 The physics of gamma ray bursts and relativistic jets. *Phys. Rep*. **561**, 1–109.

Levinson, A. & Cerutti, B. 2018 Particle-in-cell simulations of pair discharges in a starved magnetosphere of a Kerr black hole. *Astron. Astrophys*. **616**, A184.

Liang, E., Clarke, T., Henderson, A., Fu, W., Lo, W., Taylor, D., Chaguine, P., Zhou, S., Hua, Y., Cen, X., Wang, X., Kao, J., Hasson, H., Dyer, G., Serratto, K., Riley, N., Donovan, M. & Ditmire, T. 2015 High e+/e- ratio dense pair creation with $10^2$1W.cm$^-$2 laser irradiating solid targets. *Sci. Rep*. **5**, 13968.

Lightman, A.P. 1982 Relativistic thermal plasmas - pair processes and equilibria. *Astrophys. J*. **253**, 842–858.

Lyutikov, M 2006 The electromagnetic model of gamma ray bursts. *New J. Phys*. **8** (7), 119–119.

Madau, P. & Thompson, C. 2000 Relativistic winds from compact gamma ray sources. I. Radiative acceleration in the klein-nishina regime. *Astrophys. J*. **534** (1), 239–247.

Martins, S.F., Fonseca, R.A., Silva, L.O. & Mori, W.B. 2009 Ion dynamics and acceleration in relativistic shocks. *Astrophys. J*. **695** (2), L189–L193.

Medvedev, M.V. & Loeb, A. 1999 Generation of magnetic fields in the relativistic shock of gamma ray burst sources. *Astrophys. J*. **526** (2), 697–706.

Mehlhaff, J.M., Werner, G.R., Uzdensky, D.A. & Begelman, M.C. 2020 Kinetic beaming in radiative relativistic magnetic reconnection: a mechanism for rapid gamma ray flares in jets. *Mon. Not. R. Astron. Soc*. **498** (1), 799–820.

Meszaros, P. & Rees, M.J. 1993 Relativistic fireballs and their impact on external matter: models for cosmological gamma ray bursts. *Astrophys. J*. **405**, 278.

Meszaros, P. & Rees, M.J. 1997 Optical and long wavelength afterglow from gamma ray bursts. *Astrophys. J*. **476** (1), 232–237.

Molvig, K. 1975 Filamentary instability of a relativistic electron beam. *Phys. Rev. Lett*. **35**, 1504–1507.

Narayan, R., Paczynski, B. & Piran, T. 1992 gamma ray bursts as the death throes of massive binary stars. *Astrophys. J*. **395**, L83.

Piran, T. 2005 The physics of gamma ray bursts. *Rev. Mod. Phys*. **76**, 1143–1210.

Poder, K., *et al.* 2018 Experimental signatures of the quantum nature of radiation reaction in the field of an ultraintense laser. *Phys. Rev.* X **8**, 031004.

Racusin, J.L., Liang, E.W., Burrows, D.N., Falcone, A., Sakamoto, T., Zhang, B.B., Zhang, B., Evans, P. & Osborne, J. 2009 Jet breaks and energetics of Swift gamma ray burst x-ray afterglows. *Astrophys. J*. **698** (1), 43–74.

Rees, M.J. & Meszaros, P. 1994 Unsteady outflow models for cosmological gamma ray bursts. *Astrophys. J*. **430**, L93.

SAMPATH, A., *et al.* 2021 Extremely dense gamma ray pulses in electron beam-multifoil collisions. *Phys. Rev. Lett*. **126**, 064801.

SARRI, G., PODER, K., COLE, J., SCHUMAKER, W., DI PIAZZA, A., REVILLE, B., DORIA, D., DROMEY, B., GIZZI, L., GREEN, A., GRITTANI, G., KAR, S., KEITEL, C.H., KRUSHELNICK, K., KUSHEL, S., MANGLES, S., NAJMUDIN, Z., THOMAS, A.G.R., VARGAS, M. & ZEPF, M. 2015 Generation of a neutral, high-density electron-positron plasma in the laboratory. *Nat. Commun*. **6**.

SILVA, L.O., FONSECA, R.A., TONGE, J.W., DAWSON, J.M., MORI, W.B. & MEDVEDEV, M.V. 2003 Interpenetrating plasma shells: near-equipartition magnetic field generation and nonthermal particle acceleration. *Astrophys. J*. **596** (1), L121–L124.

SILVA, L.O., FONSECA, R.A., TONGE, J.W., MORI, W.B. & DAWSON, J.M. 2002 On the role of the purely transverse Weibel instability in fast ignitor scenarios. *Phys. Plasmas* **9** (6), 2458–2461.

SPITKOVSKY, A. 2008 Particle acceleration in relativistic collisionless shocks: fermi process at last? *Astrophys. J*. **682** (1), L5–L8.

STERN, B.E. 2003 Electromagnetic catastrophe in ultrarelativistic shocks and the prompt emission of gamma ray bursts. *Mon. Not. R. Astron. Soc*. **345** (2), 590–600.

THOMPSON, C. & MADAU, P. 2000 Relativistic winds from compact gamma ray sources. II. Pair loading and radiative acceleration in gamma ray bursts. *Astrophys. J*. **538** (1), 105–114.

UZDENSKY, D.A. 2011 Magnetic reconnection in extreme astrophysical environments. *Space Sci. Rev*. **160** (1), 45–71.

XU, T., SHEN, B., XU, J., LI, S., YU, Y., LI, J., LU, X., WANG, C., WANG, X., LIANG, X., LENG, Y., LI, R. & XU, Z. 2016 Ultrashort megaelectronvolt positron beam generation based on laser-accelerated electrons. *Phys. Plasmas* **23** (3), 033109.

YANG, T.Y.B., ARONS, J. & LANGDON, A.B. 1994 Evolution of the Weibel instability in relativistically hot electron–positron plasmas. *Phys. Plasmas* **1** (9), 3059–3077.

ZHANG, B. & YAN, H. 2010 The internal collision induced magnetic reconnection and turbulence (ICMART) model of gamma ray bursts. *Astrophys. J*. **726** (2), 90.